Superionic lithium transport via multiple coordination environments defined by two anion packing

Guopeng Han[1], Andrij Vasylenko[1], Luke M. Daniels[1], Chris M. Collins[1], Lucia Corti[1,2], Ruiyong Chen[1], Hongjun Niu[1], Troy D. Manning[1], Dmytro Antypov[1,2], Matthew S. Dyer[1,2], Jungwoo Lim[1,3], Marco Zanella[1], Manel Sonni[1], Mounib Bahri[4], Hongil Jo[1,2], Yun Dang[1], Craig M. Robertson[1], Frédéric Blanc[1,2,3], Laurence J. Hardwick[1,2,3], Nigel D. Browning[4,5], John B. Claridge[1,2]*, Matthew J. Rosseinsky[1,2]*

Affiliations:

[1]Department of Chemistry, University of Liverpool, Crown Street, Liverpool, L69 7ZD, United Kingdom

[2]Leverhulme Research Centre for Functional Materials Design, Materials Innovation Factory, 51 Oxford Street, University of Liverpool, Liverpool, L7 3NY, United Kingdom

[3]Stephenson Institute for Renewable Energy, University of Liverpool, Liverpool, L69 7ZF, United Kingdom

[4]Albert Crewe Centre, University of Liverpool, Research Technology Building, Elisabeth Street, Pembroke Place, Liverpool L69 3GE, United Kingdom

[5]School of Engineering, Department of Mechanical, Materials and Aerospace Engineering, University of Liverpool, Liverpool L69 3GH, United Kingdom

*Corresponding Authors: J.B.Claridge@liverpool.ac.uk, M.J.Rosseinsky@liverpool.ac.uk

Abstract: Fast cation transport in solids underpins energy storage. Materials design has focused on structures that can define transport pathways with minimal cation coordination change, restricting attention to a small part of chemical space. Motivated by the greater structural diversity of binary intermetallics than that of the metallic elements, we use two anions to build a pathway for three-dimensional superionic lithium ion conductivity that exploits multiple cation coordination environments. $Li_7Si_2S_7I$ is a pure lithium ion conductor created by an ordering of sulphide and iodide that combines elements of hexagonal and cubic close-packing analogously to the structure of NiZr. The resulting diverse network of lithium positions with distinct geometries and anion coordination chemistries affords low barriers to transport, opening a large structural space for high cation conductivity.

One-Sentence Summary: Ordering of sulphide and iodide builds a fast transport path of diverse lithium coordination geometries and anion neighbors.

Main Text: The discovery of high-performance inorganic crystalline solid-state Li^+ ion electrolytes remains a challenge to facilitate the development of next-generation battery technologies (*1-3*). The high ionic conductivity of solid electrolytes at room temperature is critical to cell performance, to ensure a low cell resistance and a high loading of active materials in the cathode composite without competing electronic conductivity. In addition, good chemical

compatibility between the solid electrolyte and Li metal is required, which would enable the use of a lithium anode to afford higher energy densities (*4*). A small number of established structural families give rise to current state-of-the-art solid Li^+ ion conductors that exhibit comparable ionic conductivities to liquid electrolytes ($\approx 10^{-2}$ S cm^{-1}). Examples include $Li_{10}GeP_2S_{12}$ (*5, 6*), $Li_{6.6}Si_{0.6}Sb_{0.4}S_5I$ (*7*) and $Li_7P_3S_{11}$ (*8*). The structures of each of these families create transport paths that minimise changes in cation coordination, which has been suggested as the origin of their high conductivities (*9-11*). This has led to materials design emphasising anion packings that afford predominantly or solely a single type of lithium coordination environment, which restricts the available chemical space. Using a different design strategy that employs multiple anions to construct suitable pathways, we synthesise a material where many different cation coordination environments combine to create superionic conductivity. This greatly expands the number and type of potential structures that can support high cation mobility.

The search for materials that define transport pathways with homogeneous cation coordination has emphasised the role of tetrahedral lithium sites (*12, 13*). In particular, attention has focussed on body-centred cubic (bcc) arrangements of anions, which enable the formation of percolating Li^+ pathways that consist of energetically equivalent face-sharing tetrahedral sites yielding low activation energies for migration (*14-17*). Bcc-like anion arrangements, which are rare because of the low density that leads them to favour cation mobility, are adopted by high-performance Li^+ ion conductors such as $Li_{10}GeP_2S_{12}$ and $Li_7P_3S_{11}$ (*14*). The A_7TX_6 (e.g., A = Li, Ag, Cu, T = P, X = S) argyrodite structure, has a tetrahedrally close-packed anion arrangement (*18-20*) that produces solely tetrahedral interstitial sites. While this fits the structure-property relationship proposed for high cation mobility, it is notable that the tetrahedral close packing of the anions in argyrodite is that of the metals in intermetallic Laves phases such as $MgCu_2$ (Fig. 1A), which are known to exhibit many other properties of interest including hydrogen uptake and mobility within the interstitial space (*21, 22*).

The anion arrangements that define the cation sites in other high-performance Li^+ ion conductors can also be closely related to known intermetallic nets. The anion sublattice of $Li_{10}GeP_2S_{12}$ is related to the As net of Cu_3As (Fig. 1B) (*5, 23*). This is not limited to sulphides. The oxide anion framework of the lithium ion-conducting garnet $Li_7La_3Zr_2O_{12}$ can be compared to the Bi framework of Bi_4Rh (Fig. 1C), while La^{3+} occupies the same site as Rh (*24, 25*).

Anion packings with precedent in the structures of intermetallic compounds can thus generate mobility pathways that require minimal coordination change based on tetrahedral interstitial cation sites. As several properties must be optimised to yield a viable electrolyte, it would be helpful to expand the potential materials design space to harness pathways exploiting the widest possible range of lithium sites. The structural diversity of intermetallics, where multiple elements with distinct chemistries take part in the sphere packing, describes a far wider range of interstitial environments that enable transport (*26, 27*). This raises the possibility of more complex anion packings that are based on intermetallics and do not rely on a single coordination geometry for lithium mobility. A high lithium mobility material may be considered as an anion packing supported by a localised framework-forming cationic species M that interacts covalently with the anions to provide chemical stability. Noting that intermetallics such as Ti_2Ni describe multiple interstitial sites with a range of coordination environments that enable hydrogen transport and uptake (*28*), we can envisage packing multiple anions in this way to generate transport pathways connecting diverse lithium sites via low barriers (Fig. 1D). Discovery synthesis that explores the connection between the large structural space established for intermetallic bonding and the creation of an equivalent space in ionic materials then offers a route to expand the small number of parent structures that afford superionic ionic conductivity by creating transport paths that feature

the full range of lithium coordination.

Results and Discussion

Element Selection and Material Synthesis

We target complex packings that tailor the coordination at multiple distinct interstitial cation sites
to optimise transport by using the size and charge diversity offered by multiple anions to replicate
the bonding diversity of intermetallics (Fig. 1D). This motivates the experimental exploration of
quaternary phase fields defined by Li^+, a suitable cation-forming element M, and two anions (X,
X′). Consideration of appropriate abundance, toxicity and electronic structure restricts the
unexplored Li-M-X-X′ chemical space to 296 phase fields (Supplementary Materials and
Methods). Our exact selection of elements from this set was informed by a variational autoencoder
(VAE) (29). The VAE operates at the level of combinations of elements, encoded by their chemical
characteristics. It is trained to recognize patterns of similarity between 2021 synthetically
accessible M-M'-X-X' phase fields reported as containing experimentally realised materials in
(30), and, based on the resulting latent space, quantitatively ranks unexplored chemistries
according to their likelihood of containing new compounds. The VAE ranks Li-Si-S-Cl, Li-Si-S-
Br and Li-Si-S-I phase fields 1st, 3rd and 9th, respectively within the selected chemical space, and
we therefore selected Li-Si-S-halogen chemistry for exploration. Structural considerations
focussed attention on the Li-Si-S-I phase field that maximizes the difference in anion size (S^{2-} $r =$
1.84 Å vs Cl^- $r =$ 1.81 Å, Br^- $r =$ 1.95 Å, I^- $r =$ 2.2 Å) and thus strengthens the connection to
complex sphere packings driven by distinct structural roles of the anions involved, in analogy to
intermetallic binaries (31). The impact of utilizing anions distinct in size and chemistry has been
recently highlighted for Li- and Na-rich anti-perovskites (32, 33). Computational exploration of
the Li-Si-S-I phase field with probe structure prediction (34-36) indicates a synthetically-
accessible low energy region of compositional space, which was targeted experimentally (Fig. S1).

Solid state syntheses for the compositions in this low energy region were carried out in carbon
crucibles inside evacuated fused silica ampoules, with the resulting phase assemblages identified
by X-ray diffraction (XRD). These measurements indicated the formation of a phase that could
not be matched to any known materials in the Li-Si-S-I field, and suitable crystals for single crystal
diffraction were grown by crystallisation of Li_2S, LiI, and elemental Si from an elemental S flux
(Supplementary Materials and Methods). The crystal structure of a new phase, $Li_7Si_2S_7I$ (LSSI),
was solved in monoclinic $P2_1/n$ symmetry using high-resolution synchrotron single crystal XRD
data collected at beamline I19, Diamond Light Source (Tables S2-6). Phase pure powder samples
of $Li_7Si_2S_7I$ were synthesised by combining SiS_2, Li_2S and LiI, using a 5% excess of SiS_2 that
avoids formation of Li_2SiS_3 and Li_4SiS_4, and heating to 723 K for 4 days with 20 K min^{-1} heating
rate and intermediate grinding after 2 days (Supplementary Materials and Methods, Figs. S2-5).
Compositional analysis via CHNS and ICP methods gives a measured composition of
$Li_{6.9(2)}Si_{2.050(5)}S_{6.96(3)}I_{0.95(1)}$, which is consistent with $Li_7Si_2S_7I$ determined from single crystal XRD
(Table S7).

Crystal Structure

The anion packing of $Li_7Si_2S_7I$ can be connected to the TlI (B33) type structures, such as the binary
intermetallic NiZr (37). The intermetallic net in NiZr is intermediate between the well-known
hexagonal and square nets (3^6 and 4^4 in Schläfli notation, respectively) and is in fact a $3^3.4^2$ semi-
regular net. A close-packed 3^6 layer is transformed by shearing every other row of triangles (Fig.
2A) to produce rows of triangles and quadrilaterals that alternate perpendicular to the shear
direction (38). Every sphere in the resulting $3^3.4^2$ layer is five-coordinate and takes part in three

3

edge-sharing triangles and two edge-sharing quadrilaterals. In the anion packing of $Li_7Si_2S_7I$, S^{2-} and I^- are ordered over the nodes of the $3^3.4^2$ net (Fig. 2B), producing pure S^{2-} (S_4) and mixed S^{2-}/I^- (S_3I) rows of spheres that run along the shear direction (the c axis) and alternate perpendicular to it in the ac plane.

5   These sheared layers stack in an ABAB sequence, similar to the hydride of NiZr (*39*) (Fig. S6), along b that places each I^- between the centroids of S_3I quadrilaterals in both neighbouring layers (Fig. 2C). This creates a 13-coordinate environment for the larger I^- that arises from the quadrilaterals produced by the shear. The quadrilaterals involved are the largest of the four in the unit cell and thus have an I^- vertex (Table S8), creating two columns of neighbouring I^- spheres 10 along b (Fig. 2C). All of the spheres in the S_3I rows have a coordination number (CN) of 13. The stacking also places every sphere in the S_4 rows between the centroids of superimposed triangles in the neighbouring layers in a CN of 11 (Fig. 2D, Table S6). This creates CN = 11 S_4 and CN = 13 S_3I rows (red and blue shading respectively in Fig. 2C) that stack alternately along a, and also alternate between two positions along b in a zig-zag manner.

15   The resulting anion packing can be viewed as the alternation of [0001] hexagonal close-packed (hcp) motifs and sheared face-centred cubic (fcc) [001]-like motifs along a (Fig. S7). The hcp motifs (red solid line in Fig. 2C) arise from the superposition of the triangles in next-nearest neighbour layers and are defined by an S_3I-S_4-S_4-S_3I sequence of anion rows along a. The sheared fcc [001]-like motifs (blue solid line in Fig. 2C) are produced by superposition of the quadrilaterals 20 generated by the shear, and are defined by an S_4-S_3I-S_3I-S_4 sequence along a. The $Li_7Si_2S_7I$ anion packing factor of 68.9% is higher than that of bcc-derived $Li_{10}GeP_2S_{12}$ (66.5%) and the tetrahedrally close-packed argyrodites (62.8% for Li_7PS_6 and 67.1% for Li_6PS_5I).

    The NiZr intermetallic exhibits extensive H uptake (*39*), which reflects the large number of available interstitial sites generated by the packing of $3^3.4^2$ semi-regular nets. Similarly, the anion 25 topology in $Li_7Si_2S_7I$ generates a diverse array of interstitial sites that emerge from the octahedral (O) and tetrahedral (T) geometries expected in simple close-packing (Figs. 3A-E and S8, Table S9). Within the hcp motif, the O_{hcp} sites share faces with each other along the triangle stacking direction b, as do the T_{hcp} sites. In the shear-derived fcc-like motif, O_{fcc} and T_{fcc} sites share edges and corners, respectively, while O_{fcc} sites share faces with T_{fcc} neighbours (Fig. 3D). O_{hcp} and O_{fcc} 30 sites, and T_{hcp} and T_{fcc} sites, share faces along a (Fig. S9), which combines the hcp and fcc-like motifs into the extended structure of $Li_7Si_2S_7I$.

    Silicon was selected as part of the chemical space for experimental exploration because of its role in defining a stable anion framework through strong localised bonding. As the smallest cation present (Si^{4+} $r = 0.26$ Å, Li^+ $r = 0.59$ Å), Si^{4+} occupies the tetrahedral voids in the hcp layer that 35 are solely coordinated by S^{2-} i.e., $T1_{hcp}$, which is the smallest tetrahedral site in the structure and located far from the large I^- anions (Table S10). The two occupied $T1_{hcp}$ sites ($T1a_{hcp}$) share corners to form Si_2S_7 dimers (Figs. 3B-E).

    The arrangement of Si^{4+} and I^- then directs the occupancy of the other sites by Li^+. The interstitial sites that share faces with the Si_2S_7 dimers are empty for electrostatic repulsion reasons (Figs. 3E, 40 S8). All four remaining T_{hcp} voids within the hcp motif have S_3I coordination ($T2_{hcp}$) and are partially occupied (between 9.8 and 50.3%) by Li^+. Of the remaining three O_{hcp} sites (Tables S9, S11), $O2_{hcp}$ with S_5I coordination is fully occupied by Li^+, while the two S_6-defined $O1_{hcp}$ sites accommodate three disordered Li^+ sites; one at the octahedron centre and two S_4-coordinated positions displaced towards the triangular faces shared with two neighbouring $T2_{hcp}$ sites (Fig. 3E). 45 This forms chains of disordered, partially occupied Li^+ sites with short Li–Li distances in the range 0.943(12) to 1.34(3) Å. All four types of octahedral site in the sheared layer are occupied by Li^+,

4

while all eight tetrahedral sites are unoccupied – the two with S_3I coordination, which is favoured in the hcp motif, appear too small to accommodate lithium in the sheared fcc-like motif (Fig. S8, Table S10). Two of the octahedral sites ($O1a_{fcc}$ with S_6 coordination and $O2_{fcc}$ with S_5I coordination) accommodate more than one Li^+ position in a disordered manner (Fig. 3E). The mixed anion packing thus creates an interconnected set of fifteen crystallographically distinct lithium positions distributed across partially occupied interstitial sites featuring extensive positional disorder over four-, five- and six-coordinate geometries defined by varying anion coordination (Tables S5, S9). Although this site diversity, large unit cell and low symmetry contrast strongly with current high-conductivity families, such a structure would be a strong candidate for high lithium mobility if the wide site distribution implied a flat potential landscape.

Transport Properties

AC impedance measurements on sintered pellets with blocking Au electrodes show that phase pure $Li_7Si_2S_7I$ has a total conductivity of $1.01(4) \times 10^{-2}$ S cm^{-1} at 303 K (Fig. 4A). The electronic contribution to the total conductivity is negligible ($\approx 10^{-10}$ S cm^{-1}, measured by DC polarisation, Fig. S11). The Arrhenius plots (Figs. 4A, S12) show two temperature ranges with different activation energies for the total conductivity: 0.204(4) eV between 303 and 373 K, and 0.58(3) eV for the total and 0.38(3) eV for the bulk conductivity between 237 and 293 K. The activation energy of 0.204(4) eV is comparable with the lowest observed (0.20-0.34 eV) for argyrodite and $Li_{10}GeP_2S_{12}$ solid electrolytes (5, 40, 41). The structural transition (Figs. 4B, S13-14) that depopulates two S_3I-defined tetrahedral and one S_6-defined octahedral Li^+ sites within the hcp motif of $Li_7Si_2S_7I$ between 237 and 293 K is associated with the reduced ionic conductivity and increased activation energy, consistent with coordination environment diversity enabling high mobility.

During linear sweep voltammetry measurements, no significant reaction currents were detected within 10 V vs. Li^+/Li in a "stainless steel (SS)|$Li_7Si_2S_7I$|Li" configuration (red curve in Fig. S15B). An oxidative decomposition potential of 2.5 V vs. Li^+/Li was observed for $Li_7Si_2S_7I$ (black curve in Fig. S15B) when using a "$Li_7Si_2S_7I$ + carbon fiber (CF)|$Li_7Si_2S_7I$|Li" configuration. Steady Li plating/stripping on a Li|$Li_7Si_2S_7I$|Li cell has been observed over 240 h at 0.05 and 0.1 mA cm^{-2} (Fig. 4C), indicating a reasonably stable $Li_7Si_2S_7I$|Li interface (Figs. S16-18). Stable cycling of $Li_7Si_2S_7I$ as the solid electrolyte within an all-solid-state cell was demonstrated against both the Li anode and $LiCoO_2$ cathode (Fig. S19). The excellent lithium transport properties are further demonstrated by the low temperature (T_{onset} of ~179 K i.e., below the temperature at which the total conductivity decreases) of the ^7Li NMR resonance line narrowing (Fig. 4D) which is comparable to the fast Li^+ ion conductors within the structural families discussed above (42-44). Modelling of the diffusion-induced ^7Li spin lattice relaxation rate behaviours (Fig. 4E), as described in the Supplementary Methods, captures both short and long range Li^+ bulk ion transport in $Li_7Si_2S_7I$, and also determines two different activation energies in the same temperature ranges as the conductivity measurements: 0.24(2) and 0.08(1) eV respectively below and above ~295 K for short range Li^+ ion mobility (black data in Fig. 4E), and 0.29(2) eV (comparable to the bulk conductivity value of 0.38(3) eV measured by AC impedance at low T) and 0.22(4) eV below and above ~295 K respectively for long range Li^+ ion mobility (coloured data in Fig. 4E). Critically, the ^7Li spin lattice relaxation rates in the rotating frame $T_{1\rho}^{-1}$ are independent of the spin-lock frequencies on the high temperature flank of the relaxation data (45, 46) (coloured data above ~295

K in Fig. 4E), which is strong experimental evidence for three dimensional (3D) long range Li^+ transport in $Li_7Si_2S_7I$.

Ion transport mechanism

In contrast with the three tetrahedral and one trigonal bipyramidal environments in highly conductive argyrodites (*47*), and the three tetrahedral and one octahedral environments in $Li_{10}GeP_2S_{12}$ (*48*), $Li_7Si_2S_7I$ has significantly more Li^+ site diversity arising from the structure-defining Si_2S_7 and I^- components. The fifteen distinct Li^+ positions in $Li_7Si_2S_7I$ are located on S_3I tetrahedral, and S_3I_3, S_5I and S_6 octahedral interstitial sites and correspond to ten different local modes of coordination (Table S9). Ab initio molecular dynamics (AIMD) simulations were performed on $Li_7Si_2S_7I$ at 400, 450 and 500 K (Supplementary Methods) to identify transport paths and the associated free energy landscape (Fig. S29). These simulations demonstrate that all 15 occupied and 12 out of 13 available Li^+ sites participate in ion transport (Fig. 5, Tables S15-17). Among the 162 distinct site-to-site connections observed to contribute to lithium transport, there were 11 low-barrier (under 0.2 eV) connections enabling rapid ionic motion within distinct units (Figs. 5C, S29), with 3D transport established between these units and all the remaining Li sites through an additional 18 connections with absolute barriers of 0.2-0.3 eV (Figs. S27-30). The arising vast array of migration options generated by the multiple low-barrier connections between the large number of chemically distinct accessible sites enables the fast transport observed in the complex, low symmetry structure of $Li_7Si_2S_7I$. The theoretical activation energy for Li^+ transport in $Li_7Si_2S_7I$ of 0.16(1) eV extracted from the mean squared displacements across 400-500 K simulations (Fig. S22C) agrees with experimentally measured values from impedance and NMR. Using Eqs. 1-4 in the Supplementary Materials and the parameters fitted in Fig. S22D, we obtain a calculated bulk ionic conductivity extrapolated to 300 K of 0.023(9) S cm^{-1}, in good agreement with the experimentally observed value. The calculated diffusion coefficients along the crystallographic axes lie with a factor of two (Figs. S22A-B), consistent with 3D transport observed by NMR (Fig. 4E).

Conclusions

$Li_7Si_2S_7I$ (LSSI) has 3D interconnected pathways for cation mobility, linking multiple partially occupied Li^+ sites of distinct geometry, anion coordination and size with low barriers to ion transport. The high room temperature Li^+ ion conductivity of $1.01(4) \times 10^{-2}$ S cm^{-1} is combined with low electronic conductivity and compatibility with a lithium metal anode. Many optimisation strategies to enhance desirable combinations of these properties are available, such as the introduction of anion disorder and the suppression by substitution of the structural phase transition that occurs just below room temperature. The potential to implement such strategies is facilitated by the structural diversity of the material, with many distinct sites to target chemically.

The anion topology of $Li_7Si_2S_7I$ blends hexagonal and sheared cubic-like close-packing motifs to accommodate the distinct chemistries of sulphide and iodide. The high conductivity arises from a combination of Li^+ sites of widely varying geometry and anion coordination, in contrast to design strategies that focus on minimising cation coordination change. Rather than restricting design to realising only those anion packings that can create conduction pathways where coordination geometry change is minimal, we can exploit the full range of lithium coordination geometries by identifying the anion arrangements required to utilize them effectively for transport by accommodating the variations in bonding over the pathway. Diverse coordination environments in large, low symmetry cells can be tailored to create partially occupied sites of equivalent energy, offering an alternative to disorder created by high symmetry. Drawing on the vast compositional and structural diversity of the intermetallics, $Li_7Si_2S_7I$ demonstrates the opportunities for

superionic cation mobility in the rich design space of multiple anion packings directed by framework-forming elements that afford strong covalent bonds. The extensive site diversity produces many different low-barrier site-to-site connections, affording multiple rapid transport pathways. Such materials are accessible through the design principles embodied in Fig. 1D that are well-suited to exploratory synthesis. The arising structures can readily be evaluated for potential cation mobility by considering the site distributions within them and computationally identifying low-barrier paths between these sites.

References and Notes

1. A. Kondori *et al.*, A room temperature rechargeable Li_2O-based lithium-air battery enabled by a solid electrolyte. *Science* **379**, 499-505 (2023).
2. Z. Ning *et al.*, Visualizing plating-induced cracking in lithium-anode solid-electrolyte cells. *Nat. Mater.* **20**, 1121-1129 (2021).
3. F. Marchini *et al.*, The hidden side of nanoporous β-Li_3PS_4 solid electrolyte. *Adv. Energy. Mater.* **11**, 2101111 (2021).
4. A. M. Abakumov, S. S. Fedotov, E. V. Antipov, J.-M. Tarascon, Solid state chemistry for developing better metal-ion batteries. *Nat. Commun.* **11**, 4976 (2020).
5. N. Kamaya *et al.*, A lithium superionic conductor. *Nat. Mater.* **10**, 682-686 (2011).
6. J. A. Dawson, M. S. Islam, A nanoscale design approach for enhancing the Li-ion conductivity of the $Li_{10}GeP_2S_{12}$ solid electrolyte. *ACS Mater. Lett.* **4**, 424-431 (2022).
7. L. Zhou, N. Minafra, W. G. Zeier, L. F. Nazar, Innovative approaches to Li-argyrodite solid electrolytes for all-solid-state lithium batteries. *Acc. Chem. Res.* **54**, 2717-2728 (2021).
8. H. Yamane *et al.*, Crystal structure of a superionic conductor, $Li_7P_3S_{11}$. *Solid State Ion.* **178**, 1163-1167 (2007).
9. R. D. Armstrong, R. S. Bulmer, T. Dickinson, Some factors responsible for high ionic conductivity in simple solid compounds. *J. Solid State Chem.* **8**, 219-228 (1973).
10. J. C. Bachman *et al.*, Inorganic solid-state electrolytes for lithium batteries: mechanisms and properties governing ion conduction. *Chem. Rev.* **116**, 140-162 (2016).
11. Q. Zhang *et al.*, Sulfide-based solid-state electrolytes: synthesis, stability, and potential for all-solid-state batteries. *Adv. Mater.* **31**, 1901131 (2019).
12. H. Fang, P. Jena, Argyrodite-type advanced lithium conductors and transport mechanisms beyond paddle-wheel effect. *Nat. Commun.* **13**, 2078 (2022).
13. Y. Zeng *et al.*, High-entropy mechanism to boost ionic conductivity. *Science* **378**, 1320-1324 (2022).
14. Y. Wang *et al.*, Design principles for solid-state lithium superionic conductors. *Nat. Mater.* **14**, 1026-1031 (2015).
15. A. Y. S. Eng *et al.*, Theory-guided experimental design in battery materials research. *Sci. Adv.* **8**, eabm2422 (2022).
16. A. Banik *et al.*, On the underestimated influence of synthetic conditions in solid ionic conductors. *Chem. Sci.* **12**, 6238-6263 (2021).
17. S. P. Culver, R. Koerver, T. Krauskopf, W. G. Zeier, Designing ionic conductors: the interplay between structural phenomena and interfaces in thiophosphate-based solid-state batteries. *Chem. Mater.* **30**, 4179-4192 (2018).
18. W. F. Kuhs, R. Nitsche, K. Scheunemann, The argyrodites — a new family of tetrahedrally close-packed structures. *Mater. Res. Bull.* **14**, 241-248 (1979).

19. S.-T. Kong *et al.*, Lithium argyrodites with phosphorus and arsenic: order and disorder of lithium atoms, crystal chemistry, and phase transitions. *Chem. Eur. J.* **16**, 2198-2206 (2010).

20. B. J. Morgan, Mechanistic origin of superionic lithium diffusion in anion-disordered Li_6PS_5X argyrodites. *Chem. Mater.* **33**, 2004-2018 (2021).

21. R. L. Berry, G. V. Raynor, The crystal chemistry of the Laves phases. *Acta Crystallogr.* **6**, 178-186 (1953).

22. D. Ivey, D. Northwood, Hydrogen site occupancy in AB_2 Laves phases. *J. Less. Common. Met.* **115**, 23-33 (1986).

23. J. E. Iglesias, W. Nowacki, Refinement of the crystal structure of α domeykite, a structure related to the A15 type. *Z. Kristallogr. - Cryst. Mater.* **145**, 334-345 (1977).

24. C. A. Geiger *et al.*, Crystal chemistry and stability of "$Li_7La_3Zr_2O_{12}$" garnet: a fast lithium-ion conductor. *Inorg. Chem.* **50**, 1089-1097 (2011).

25. R. G. Ross, W. Hume-Rothery, The compound Bi_4Rh. *J. Less. Common. Met.* **1**, 304-308 (1959).

26. M. Hirscher *et al.*, Materials for hydrogen-based energy storage – past, recent progress and future outlook. *J. Alloys Compd.* **827**, 153548 (2020).

27. T. G. Akhmetshina, V. A. Blatov, D. M. Proserpio, A. P. Shevchenko, Topology of intermetallic structures: from statistics to rational design. *Acc. Chem. Res.* **51**, 21-30 (2018).

28. H. Buchner, M. A. G. , K.-D. Beccu, H. Säufferer, Wasserstoff in intermetallischen phasen am beispiel des systems Titan-Nickel-Wasserstoff. *Int. J. Mater. Res.* **63**, 497-500 (1972).

29. A. Vasylenko *et al.*, Element selection for crystalline inorganic solid discovery guided by unsupervised machine learning of experimentally explored chemistry. *Nat. Commun.* **12**, 5561 (2021).

30. D. Zagorac, H. Muller, S. Ruehl, J. Zagorac, S. Rehme, Recent developments in the Inorganic Crystal Structure Database: theoretical crystal structure data and related features. *J. Appl. Cryst.* **52**, 918-925 (2019).

31. R. D. Shannon, Revised effective ionic radii and systematic studies of interatomic distances in halides and chalcogenides. *Acta. Crystallogr. A.* **32**, 751-767 (1976).

32. K. Kim, D. J. Siegel, Correlating lattice distortions, ion migration barriers, and stability in solid electrolytes. *J. Mater. Chem. A* **7**, 3216-3227 (2019).

33. P.-C. Tsai *et al.*, Double paddle-wheel enhanced sodium ion conduction in an antiperovskite solid electrolyte. *Adv. Energy. Mater.* **13**, 2203284 (2023).

34. C. M. Collins *et al.*, Discovery of a low thermal conductivity oxide guided by probe structure prediction and machine learning. *Angew. Chem. Int. Ed.* **60**, 16457-16465 (2021).

35. C. Collins *et al.*, Accelerated discovery of two crystal structure types in a complex inorganic phase field. *Nature* **546**, 280-284 (2017).

36. D. C. Lonie, E. Zurek, XtalOpt: An open-source evolutionary algorithm for crystal structure prediction. *Comput. Phys. Commun.* **182**, 372-387 (2011).

37. M. E. Kirkpatrick, D. M. Bailey, J. F. Smith, The structures of $NiZr_2$, NiZr and their hafnium analogs. *Acta Crystallogr.* **15**, 252-255 (1962).

38. M. O'Keeffe, B. G. Hyde, Plane nets in crystal chemistry. *Philos. Trans. R. Soc. A* **295**, 553-623 (1980).

39. D. G. Westlake, Stoichiometries and interstitial site occupation in the hydrides of ZrNi and other isostructural intermetallic compounds. *J. Less. Common. Met.* **75**, 177-185 (1980).

40. P. Adeli *et al.*, Boosting solid-state diffusivity and conductivity in lithium superionic argyrodites by halide substitution. *Angew. Chem. Int. Ed.* **58**, 8681-8686 (2019).

41. Y. Kato *et al.*, High-power all-solid-state batteries using sulfide superionic conductors. *Nat. Energy.* **1**, 16030 (2016).

42. V. Epp, Ö. Gün, H.-J. Deiseroth, M. Wilkening, Highly mobile ions: low-temperature NMR directly probes extremely fast Li^+ hopping in argyrodite-type Li_6PS_5Br. *J. Phys. Chem. Lett.* **4**, 2118-2123 (2013).

43. A. Kuhn, V. Duppel, B. V. Lotsch, Tetragonal $Li_{10}GeP_2S_{12}$ and Li_7GePS_8 – exploring the Li ion dynamics in LGPS Li electrolytes. *Energy Environ. Sci.* **6**, 3548-3552 (2013).

44. D. Wohlmuth, V. Epp, M. Wilkening, Fast Li ion dynamics in the solid electrolyte $Li_7P_3S_{11}$ as probed by [6,7]Li NMR spin-lattice relaxation. *ChemPhysChem* **16**, 2582-2593 (2015).

45. C. A. Sholl, Nuclear spin relaxation by translational diffusion in liquids and solids: high- and low-frequency limits. *J. Phys. C: Solid State Phys.* **14**, 447-464 (1981).

46. A. Kuhn *et al.*, Li ion diffusion in the anode material $Li_{12}Si_7$: ultrafast quasi-1D diffusion and two distinct fast 3D jump processes separately revealed by ^{7}Li NMR relaxometry. *J. Am. Chem. Soc.* **133**, 11018-11021 (2011).

47. L. Zhou, A. Assoud, Q. Zhang, X. Wu, L. F. Nazar, New family of argyrodite thioantimonate lithium superionic conductors. *J. Am. Chem. Soc.* **141**, 19002-19013 (2019).

48. A. Kuhn, J. Köhler, B. V. Lotsch, Single-crystal X-ray structure analysis of the superionic conductor $Li_{10}GeP_2S_{12}$. *Phys. Chem. Chem. Phys.* **15**, 11620-11622 (2013).

49. K. Momma, F. Izumi, VESTA 3 for three-dimensional visualization of crystal, volumetric and morphology data. *J. Appl. Cryst.* **44**, 1272-1276 (2011).

50. D. P. Kingma, M. Welling, Auto-encoding variational bayes. *arXiv:1312.6114*, [stat.ML] (2013).

51. D. Jha *et al.*, ElemNet: Deep learning the chemistry of materials from only elemental composition. *Sci. Rep.* **8**, 17593 (2018).

52. H. Glawe, A. Sanna, E. K. U. Gross, M. A. L. Marques, The optimal one dimensional periodic table: a modified Pettifor chemical scale from data mining. *New J. Phys.* **18**, 093011 (2016).

53. J. Gamon *et al.*, Computationally guided discovery of the sulfide Li_3AlS_3 in the Li–Al–S phase field: structure and lithium conductivity. *Chem. Mater.* **31**, 9699-9714 (2019).

54. E. Shoko *et al.*, Polymorph of $LiAlP_2O_7$: combined computational, synthetic, crystallographic, and ionic conductivity study. *Inorg. Chem.* **60**, 14083-14095 (2021).

55. A. Vasylenko *et al.*, Exploring energy-composition relationships with Bayesian optimization for accelerated discovery of inorganic materials. *arXiv:2302.00710*, [cond-mat.mtrl-sci] (2023).

56. G. Kresse, J. Hafner, Ab initio molecular dynamics for liquid metals. *Phys. Rev. B* **47**, 558-561 (1993).

57. J. P. Perdew, K. Burke, M. Ernzerhof, Generalized gradient approximation made simple. *Phys. Rev. Lett.* **77**, 3865-3868 (1996).

58. W. Sun *et al.*, The thermodynamic scale of inorganic crystalline metastability. *Sci. Adv.* **2**, e1600225 (2016).

59. S. Nosé, A unified formulation of the constant temperature molecular dynamics methods. *J. Chem. Phys.* **81**, 511-519 (1984).

60. R. Chitra, S. Yashonath, Estimation of error in the diffusion coefficient from molecular dynamics simulations. *J. Chem. Phys. B* **101**, 5437-5445 (1997).

61. Z. Deng, Z. Zhu, I.-H. Chu, S. P. Ong, Data-driven first-principles methods for the study and design of alkali superionic conductors. *Chem. Mater.* **29**, 281-288 (2017).

62. Y. Zhang, M. X. Xie, W. Zhang, J. L. Yan, G. Q. Shao, Synthesis and purification of SiS_2 and Li_2S for $Li_{9.54}Si_{1.74}P_{1.44}S_{11.7}Cl_{0.3}$ solid electrolyte in Lithium-ion batteries. *Mater. Lett.* **266**, 127508 (2020).

63. H. Nowell, S. A. Barnett, K. E. Christensen, S. J. Teat, D. R. Allan, I19, the small-molecule single-crystal diffraction beamline at Diamond Light Source. *J. Synch. Rad.* **19**, 435-441 (2012).

64. CrysAlis^{Pro} Oxford Diffraction/Agilent Technologies UK Ltd, Yarnton, England.

65. G. M. Sheldrick, SHELXT - Integrated space-group and crystal-structure determination. *Acta Cryst. A* **71**, 3-8 (2015).

66. G. M. Sheldrick, Crystal structure refinement with SHELXL. *Acta Cryst. C* **71**, 3-8 (2015).

67. O. V. Dolomanov, L. J. Bourhis, R. J. Gildea, J. A. K. Howard, H. Puschmann, OLEX2: a complete structure solution, refinement and analysis program. *J. Appl. Cryst.* **42**, 339-341 (2009).

68. A. Coelho, Whole-profile structure solution from powder diffraction data using simulated annealing. *J. Appl. Cryst.* **33**, 899-908 (2000).

69. P. A. Beckmann, C. Dybowski, A thermometer for nonspinning solid-state NMR spectroscopy. *J. Magn. Reson.* **146**, 379-380 (2000).

70. D. Johnson, *ZView: A software program for IES analysis 3.5D;* Scribner Associates Inc, (2007).

71. Z. W. Seh *et al.*, Facile synthesis of Li_2S–polypyrrole composite structures for high-performance Li_2S cathodes. *Energy Environ. Sci.* **7**, 672-676 (2014).

72. R. Rocca, M. F. Sgroi, B. Camino, M. D'Amore, A. M. Ferrari, Disordered rock-salt type Li_2TiS_3 as novel cathode for LIBs: a computational point of view. *Nanomaterials* **12**, 1832 (2022).

73. C. Chen *et al.*, Synthesis, characterization and chemical stability of silicon dichalcogenides, $Si(Se_xS_{1−x})_2$. *J. Cryst. Growth* **452**, 151-157 (2016).

74. D. E. Watson, S. W. Martin, Short range order characterization of the $Na_2S + SiS_2$ glass system using Raman, infrared and ^{29}Si magic angle spinning nuclear magnetic resonance spectroscopies. *J. Non-Cryst. Solids* **471**, 39-50 (2017).

75. A. Pradel, M. Ribes, Lithium chalcogenide conductive glasses. *Mater. Chem. Phys.* **23**, 121-142 (1989).

76. J. Zhou *et al.*, $Rb_2CdSi_4S_{10}$: novel $[Si_4S_{10}]$ T2-supertetrahedra-contained infrared nonlinear optical material with large band gap. *Mater. Horiz.* **10**, 619-624 (2023).

77. W. Xie, Y. Yun, L. Deng, G. Li, S. Pan, Second-harmonic generation-positive $Na_2Ga_2SiS_6$ with a broad band gap and a high laser damage threshold. *Inorg. Chem.* **61**, 7546-7552 (2022).

78. J. G. Hexem, M. H. Frey, S. J. Opella, Influence of ^{14}N on ^{13}C NMR spectra of solids. *J. Am. Chem. Soc.* **103**, 224-226 (1981).

79. G. A. Webb, Ed., *Chapter Three - Recent advances in chlorine, bromine, and iodine solid-state NMR spectroscopy*, (Academic Press, 2020).

80. C. M. Widdifield, D. L. Bryce, Solid-state ^{127}I NMR and GIPAW DFT study of metal iodides and their hydrates: structure, symmetry, and higher-order quadrupole-induced effects. *J. Phys. Chem. A* **114**, 10810-10823 (2010).

81. J. Lin *et al.*, A high-entropy multicationic substituted lithium argyrodite superionic solid electrolyte. *ACS Mater. Lett.* **4**, 2187-2194 (2022).

82. S. Flynn *et al.*, $LiIn_2SbO_6$: A new rutile-related structure type with unique ion channels. *Chem. Mater.* **32**, 4785-4794 (2020).

83. J. T. S. Irvine, D. C. Sinclair, A. R. West, Electroceramics: characterization by impedance spectroscopy. *Adv. Mater.* **2**, 132-138 (1990).

84. W. G. Zeier, S. Zhou, B. Lopez-Bermudez, K. Page, B. C. Melot, Dependence of the Li-ion conductivity and activation energies on the crystal structure and ionic radii in $Li_6MLa_2Ta_2O_{12}$. *ACS Appl. Mat. Interfaces* **6**, 10900-10907 (2014).

85. F. Han, Y. Zhu, X. He, Y. Mo, C. Wang, Electrochemical stability of $Li_{10}GeP_2S_{12}$ and $Li_7La_3Zr_2O_{12}$ solid electrolytes. *Adv. Energy. Mater.* **6**, 1501590 (2016).

86. T. K. Schwietert *et al.*, Clarifying the relationship between redox activity and electrochemical stability in solid electrolytes. *Nat. Mater.* **19**, 428-435 (2020).

87. J. Kasemchainan *et al.*, Critical stripping current leads to dendrite formation on plating in lithium anode solid electrolyte cells. *Nat. Mater.* **18**, 1105-1111 (2019).

88. S. Wenzel, S. J. Sedlmaier, C. Dietrich, W. G. Zeier, J. Janek, Interfacial reactivity and interphase growth of argyrodite solid electrolytes at lithium metal electrodes. *Solid State Ion.* **318**, 102-112 (2018).

89. S. Wenzel *et al.*, Direct observation of the interfacial instability of the fast ionic conductor $Li_{10}GeP_2S_{12}$ at the lithium metal anode. *Chem. Mater.* **28**, 2400-2407 (2016).

90. T.-T. Zuo *et al.*, A mechanistic investigation of the $Li_{10}GeP_2S_{12}|LiNi_{1-x-y}Co_xMn_yO_2$ interface stability in all-solid-state lithium batteries. *Nat. Commun.* **12**, 6669 (2021).

91. H. Wan *et al.*, Bifunctional interphase-enabled $Li_{10}GeP_2S_{12}$ electrolytes for lithium–sulfur battery. *ACS Energy Lett.* **6**, 862-868 (2021).

92. J. Su *et al.*, Interfacial modification between argyrodite-type solid-state electrolytes and Li metal anodes using LiPON interlayers. *Energy Environ. Sci.* **15**, 3805-3814 (2022).

93. C. Lee *et al.*, Stack pressure measurements to probe the evolution of the lithium–solid-state electrolyte interface. *ACS Energy Lett.* **6**, 3261-3269 (2021).

94. L. Marton, C. Marton, Eds., *Electron probe microanalysis*, (Academic Press, 1960).

95. J. D. Brown, Modeling of depth distribution of x-ray production. *Scan Electron Microsc* **1982**, 137-144 (1982).

96. JEOL, Energy table for EDS analysis, version 1, https://www.unamur.be/services/microscopie/sme-documents/Energy-20table-20for-20EDS-20analysis-1.pdf.

97. J. S. Waugh, E. I. Fedin, Determination of hindered-rotation barriers in solids. *Sov. Phys. Solid State* **4**, 1633-1636 (1963).

98. A. Abragam, *Principles of nuclear magnetism*, (Clarendon Press, 1983).

99. A. Steigel, H. W. Spiess, *Dynamic NMR spectroscopy*, P. Diehl, E. Fluck, R. Kosfeld, Eds., (Springer Berlin, Heidelberg, 1978).

100. A. Kuhn *et al.*, Li self-diffusion in garnet-type $Li_7La_3Zr_2O_{12}$ as probed directly by diffusion-induced ^7Li spin-lattice relaxation NMR spectroscopy. *Phys. Rev. B* **83**, 094302 (2011).

101. P. Heitjans, J. Kärger, Eds., *Diffusion in condensed matter: methods, materials, models*, (Springer Berlin, Heidelberg, 2006).

102. A. Hjorth Larsen *et al.*, The atomic simulation environment—a Python library for working with atoms. *J. Phys.: Condens. Matter* **29**, 273002 (2017).

103. K. Kang, D. Morgan, G. Ceder, First principles study of Li diffusion in I-Li_2NiO_2 structure. *Phys. Rev. B* **79**, 014305 (2009).

Author contributions: GH, AV, LMD, MSD, JBC and MJR developed the project direction. GH discovered and synthesised the material. LMD, TDM and JBC advised on the synthesis. GH, CMR, JBC, HJ and LMD characterised the crystal structure. LC and FB performed NMR measurements and analysed the data. CMC, DA and MSD carried out AIMD calculations. AV developed ML models and performed the CSP calculations. GH, HN, JL and YD performed electrochemical measurements under supervision of RC and LJH. MZ, MS, MB and NDB performed FIB-SEM measurements and analysed the data. All authors were involved in discussions and evaluations of the drafts during the writing process. MJR directed the research.

Competing interests: Authors declare no competing interests. GH, MJR, AV, LMD, JBC, TM, RC, HN and MSD are inventors for a UK patent (application No. 2302541.4, filling date 22 February 2023) filed by the University of Liverpool.

Data and materials availability: All underlying data will be published at https://datacat.liverpool.ac.uk/id/eprint/1989. The crystal structures of $Li_7Si_2S_7I$ at a range of temperatures are deposited with CSD accession codes 2244239 (100 K), 2244240 (240 K), 2244241 (300 K), 2244243 (330 K), and 2244242 (500 K).

Supplementary Materials

Materials and Methods

Supplementary Text

Figs. S1 to S30

Tables S1 to S17

References (*50-103*)
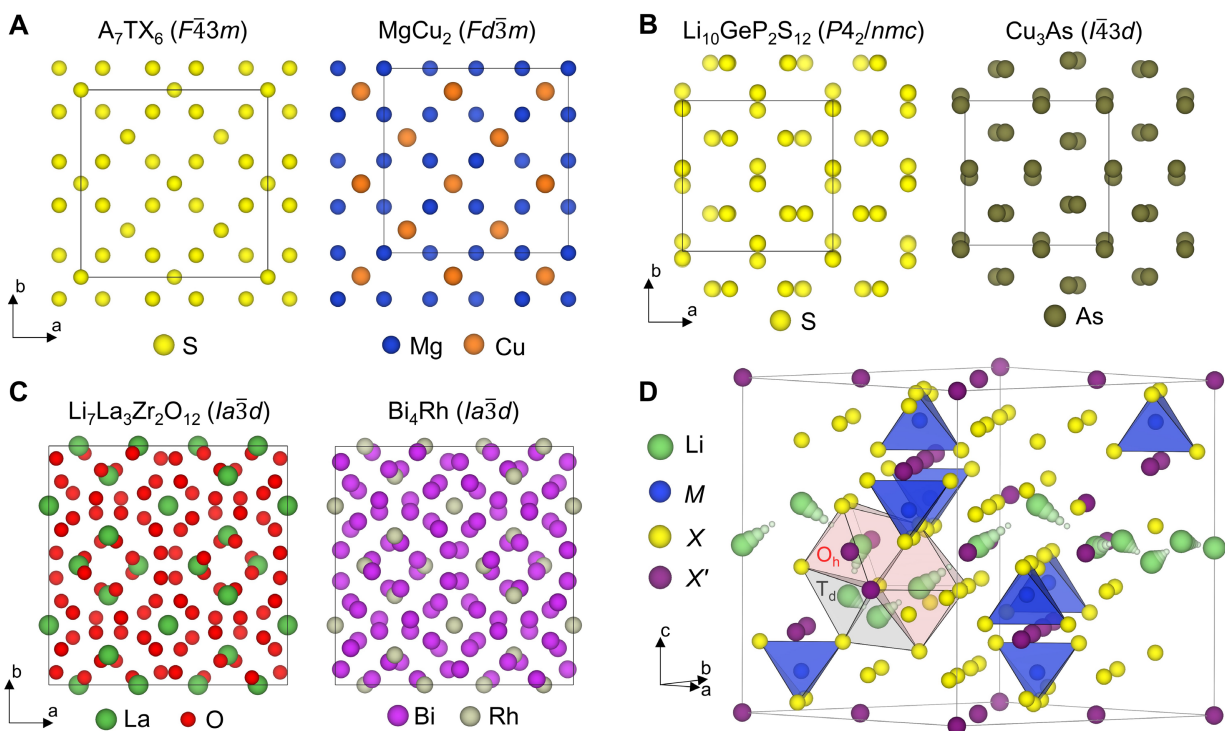
5 CIF files and their checkCIF files

Fig. 1. Ionic conductors and intermetallic nets. Comparison of the structures of high-performance Li^+ ion conductors with known intermetallic nets: (**A**) A_7TX_6 argyrodite and $MgCu_2$ Laves phase, (**B**) $Li_{10}GeP_2S_{12}$ and Cu_3As, and (**C**) $Li_7La_3Zr_2O_{12}$ garnet and Bi_4Rh. A conceptual view of the chemical components of a high lithium mobility structure is shown in (**D**) consisting of a framework-forming cation (M) and mobile Li^+ within a packing arrangement formed from two anions X and X′. This schematic is based on the packing in the binary intermetallic Ti_2Ni, with anions occupying the Ti and Ni positions, and highlights potential cation transport pathways that exploit multiple coordination environments.
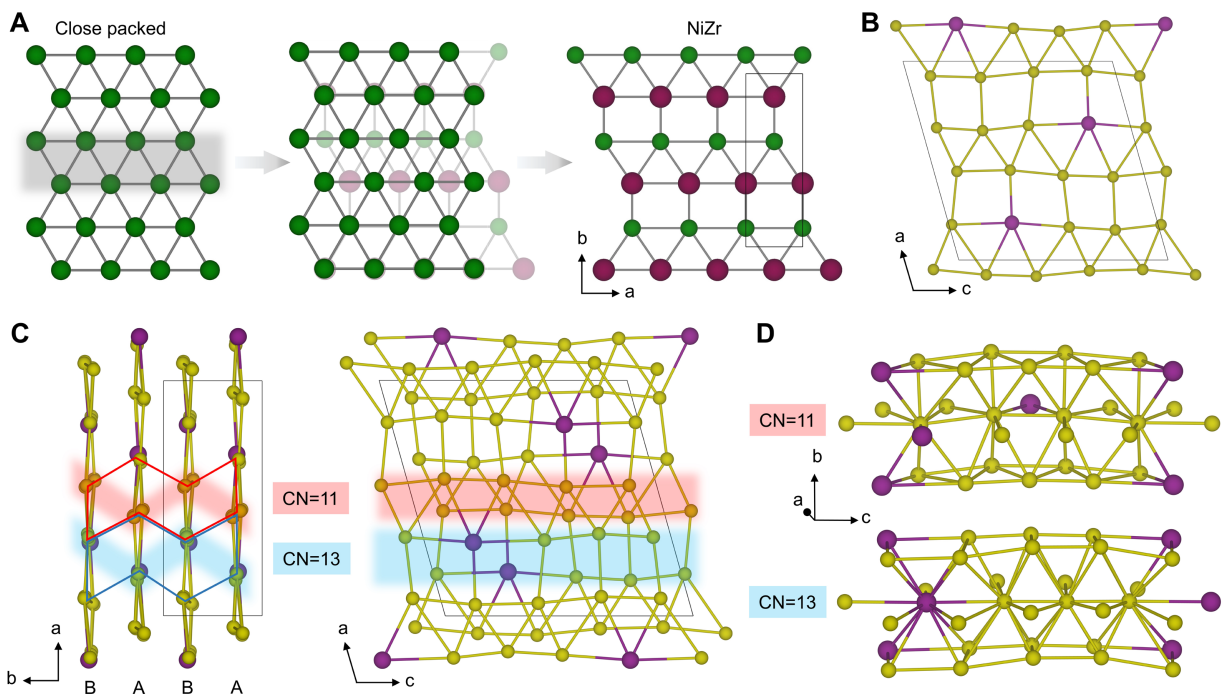
Fig. 2. Multiple anion order shears close-packed layers in Li₇Si₂S₇I. A single 3^6 close-packed layer (**A**) is transformed into the $3^3.4^2$ semi-regular net of NiZr by shearing every other row of triangles. Ni and Zr atoms are green and maroon, respectively. (**B**) Li₇Si₂S₇I has an anion topology based on NiZr where S^{2-} (yellow) and I^- (purple) are ordered in $3^3.4^2$ layers. (**C**) ABAB stacking of these layers along *b* with resulting proximity of neighbouring I^- anions produces (**D**) anion coordination spheres of 11 (S_4 rows) and 13 (S_3I rows) from superposition of triangles and quadrilaterals in neighbouring layers, respectively. The CN = 11 (red shading) and CN = 13 (blue shading) rows are stacked along *b* in a zig-zag manner to form pairs in the *bc* plane that alternate along *a*. Four rows of anions with a 13-11-11-13 (S_3I-S_4-S_4-S_3I) coordination number sequence define hcp motifs (solid red line in left part of C) that alternate with sheared fcc-like motifs (solid blue line) defined by an 11-13-13-11 (S_4-S_3I-S_3I-S_4) sequence of anion rows.
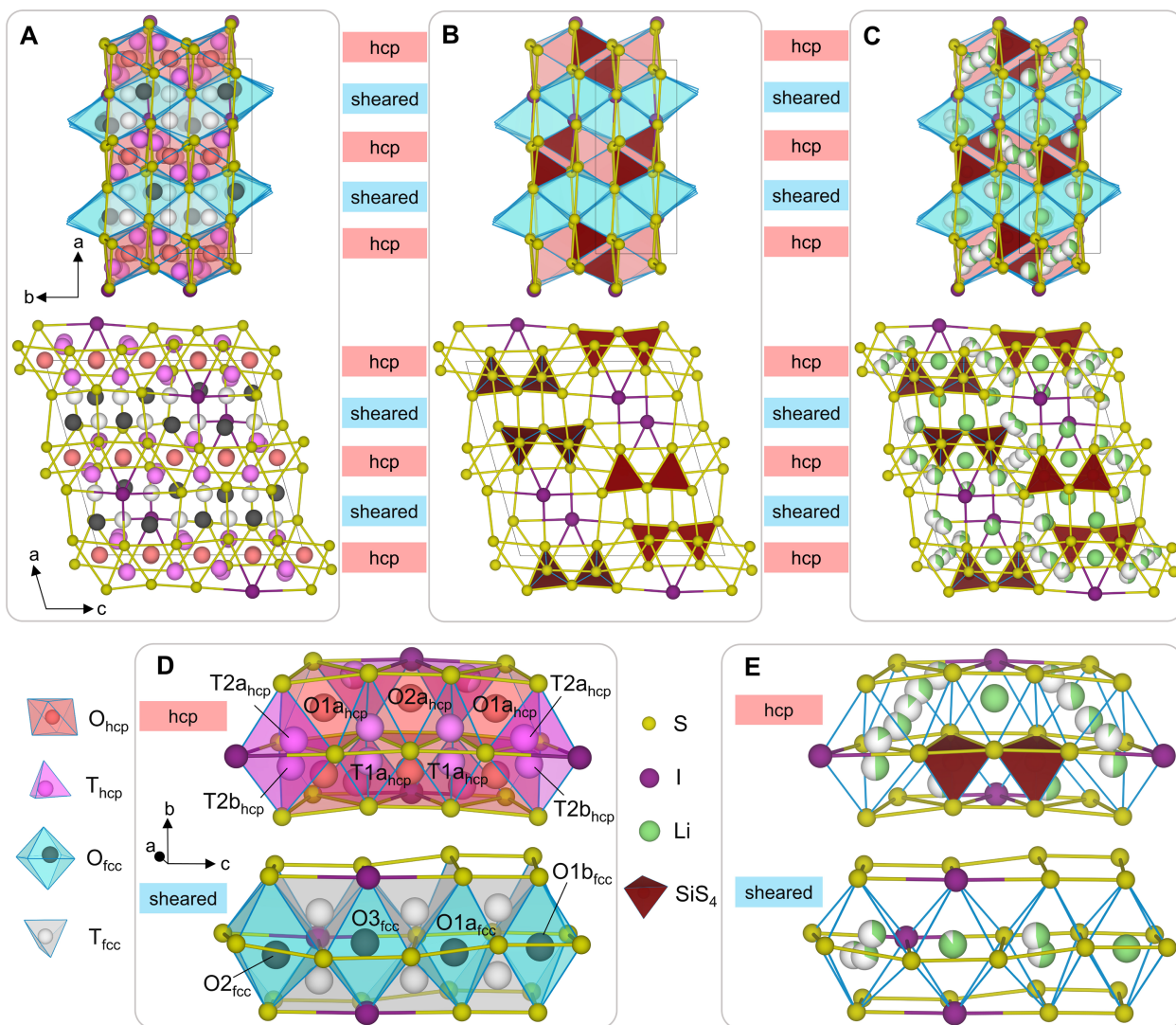
Fig. 3. Multiple coordination geometry interstitial sites and cation occupancy patterns in Li₇Si₂S₇I. The unit cell of $Li_7Si_2S_7I$ viewed along *c* and *b* shows (**A**) the available interstitial sites, (**B**) the tetrahedral sites occupied by Si^{4+} to form Si_2S_7 dimers and (**C**) the sites occupied by Si^{4+} and Li^+ (partial occupancy indicated by fraction of green shading). (**D**) shows the interstitial sites available for cation occupancy in the distinct hcp and sheared fcc-like anion motifs. (**E**) shows the sites occupied by Si^{4+} and Li^+ within $Li_7Si_2S_7I$. The interstitial sites are categorised based on their location (hcp or sheared fcc-like motifs), the coordinating anions and the connectivity to Si_2S_7 dimers (Fig. S8, Table S9). The octahedral and tetrahedral sites (O_{hcp} and T_{hcp}) in the hcp motif are red and pink respectively. The O_{fcc} and T_{fcc} sites in the sheared fcc-like motif are blue and grey, respectively. The two smallest corner-sharing tetrahedral sites formed solely by S^{2-} anions are within the hcp motif ($T1a_{hcp}$) and are occupied by Si^{4+}, forming Si_2S_7 dimers. The sites that share edges or corners with Si_2S_7 dimers are more favourable for Li^+ occupancy than those that share faces.
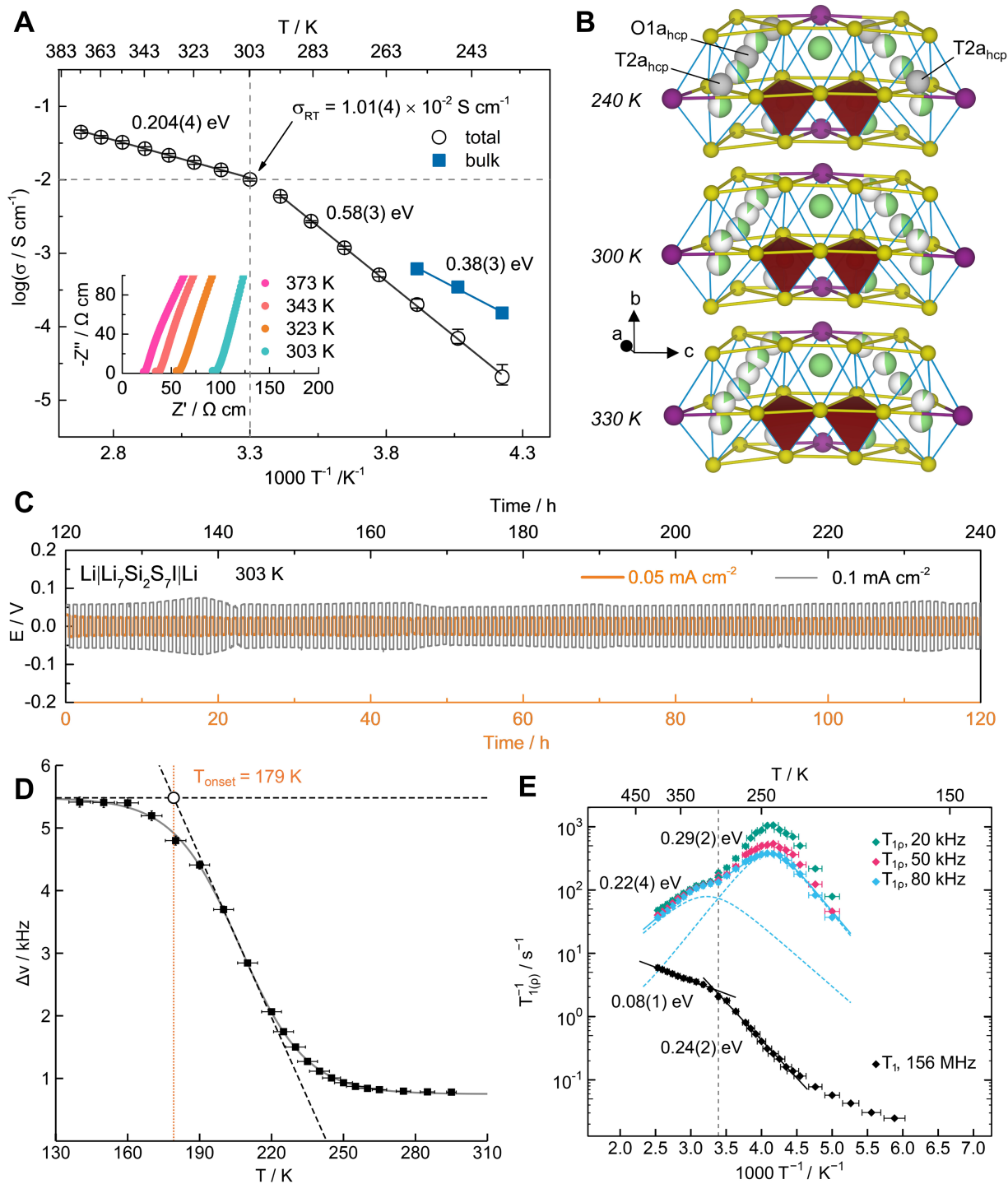
16

Fig. 4. Ionic conductivity and stability of phase pure $Li_7Si_2S_7I$. (**A**) Temperature dependence of the total and bulk conductivity of $Li_7Si_2S_7I$, with derived activation energies shown. The inset shows representative Nyquist plots between 303 and 373 K. The vertical and horizontal dashed lines highlight the room temperature conductivity. (**B**) $Li_7Si_2S_7I$ undergoes an isostructural phase transition where three of the Li^+ sites (drawn as grey spheres in the 240 K structure) observed at 300 K and above within the hcp motif become unoccupied at 240 K and below (Fig. S13). The occupancies of all Li^+ sites in $Li_7Si_2S_7I$ between 100 and 500 K are summarized in Table S12. (**C**)

Galvanostatic Li plating/stripping voltage profiles of a symmetrical Li|Li$_7$Si$_2$S$_7$I|Li cell measured at 303 K with 0.05 mA cm^{-2} for 120 h and then at 0.1 mA cm^{-2} for a further 120 h. This is measured on a phase-pure sample, not a composite with impurity phases. (**D**) Full width at half maximum of the static ^{7}Li central NMR transition Δv (black squares) as a function of temperature fitted to a Boltzmann sigmoid regression curve (grey line), highlighting the low onset temperature of line narrowing (orange line) at T_{onset} ~179 K. (**E**) ^{7}Li spin lattice relaxation rates in the laboratory frame T_1 (black diamonds) and rotating frame $T_{1\rho}$ at different spin-lock frequencies (coloured diamonds) as a function of reciprocal temperature modelled as discussed in the Supplementary Methods (only the fit to the data obtained with v_1 of 80 kHz is shown for clarity, blue dashed and solid lines indicate the individual and overall processes, respectively) to extract the activation barriers. The dashed vertical line at 295 K indicates the discontinuity in slopes observed in the rates.
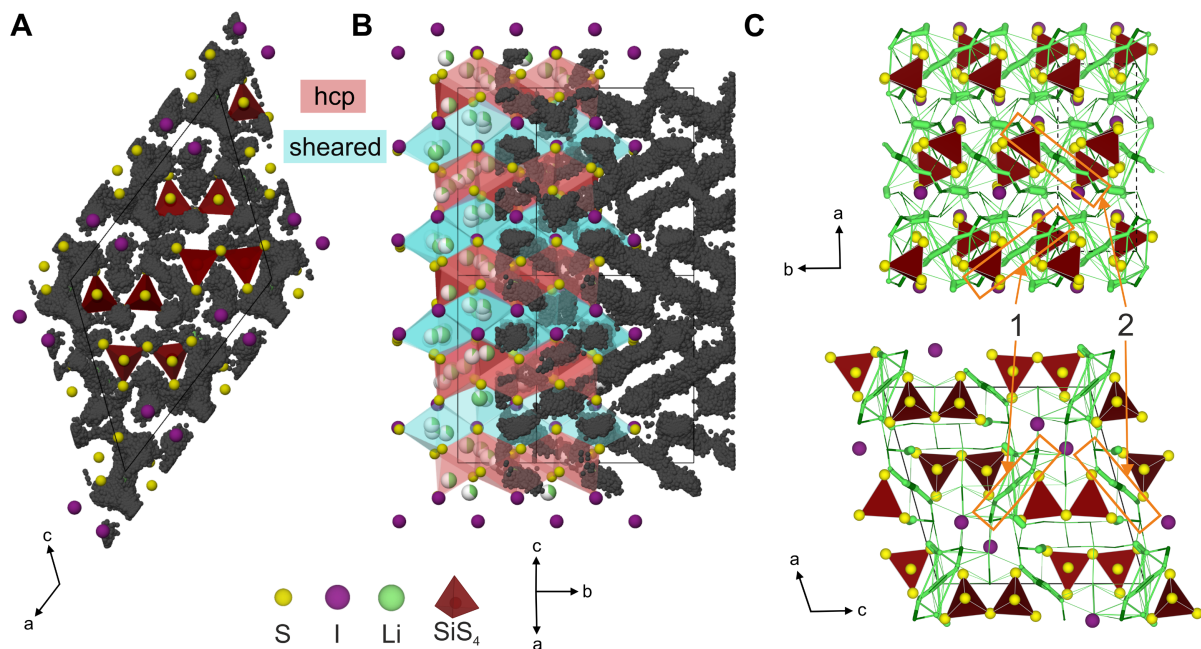
Fig. 5. Ab initio molecular dynamics (AIMD) simulation of Li₇Si₂S₇I. Projections along the (**A**) [010] and (**B**) [101] directions of the $P2_1/c$ AIMD supercell (equivalent to the [010] and [001] directions in the experimental $P2_1/n$ unit cell shown in Fig. 3C, see Supplementary Materials and Methods). The black points indicate the calculated positions of Li atoms taken at time intervals of 0.05 ps from the 300 ps AIMD simulation at 500 K. The experimental structure at 300 K is overlaid with the simulation to guide the eye to the location of the hcp and sheared fcc-like motifs in the structure. The distribution of Li atoms in the simulation supports the experimental observation that Li⁺ is highly mobile in 3D. (**C**) Migration pathways through Li₇Si₂S₇I displayed as cylinders between occupied Li (green) and available interstitial sites (dark green) in the experimental structure at 300 K. The cross section of each cylinder is proportional to the hopping frequency observed in the AIMD simulation (Fig. S26). The labelled orange boxes indicate the location of the two fast diffusion units 1 and 2 oriented in different directions within the structure. 3D transport between these units occurs through multiple connections with calculated activation barriers of 0.2 – 0.3 eV (Fig. S29).